Remote Sensing of Environment 286 (2023) 113404

Contents lists available at ScienceDirect

Remote Sensing of Environment

journal homepage: www.elsevier.com/locate/rse

Dominant timescales of variability in global satellite chlorophyll and SST revealed with a MOving Standard deviation Saturation (MOSS) approach

Bror F. Jönsson [a,*], Joseph Salisbury [b], Elizabeth C. Atwood [a], Shubha Sathyendranath [a], Amala Mahadevan [c]

[a] Plymouth Marine Laboratory, UK
[b] University of New Hampshire, USA
[c] Woods Hole Oceanographic Institution, USA

ARTICLE INFO

Keywords:
Satellite oceanography
Timescales
Biological production
Chlorophyll
Sea surface temperature
Variability

ABSTRACT

Satellite-derived sea surface temperature (SST) and chlorophyll (Chl) datasets have been invaluable for estimating the oceanic primary production, air-sea heat exchange, and the spatial and seasonal patterns in their variability. However, data gaps, resulting from clouds and other factors, reduce coverage unevenly (to just about 20%) and make it difficult to analyze the temporal variability of Chl and SST on sub-seasonal time scales. Here, we present a MOving Standard deviation Saturation (MOSS) method to enable the analysis of sparse time series (with as little as 10% of the data). We apply the method to identify the dominating (sub-annual) timescales of variability, τ_d, for SST and Chl in every region. We find that τ_d values for Chl and SST are not consistent or correlated with each other over large areas, and in general, SST varies on longer timescales than Chl, i.e. τ_d(SST) $>\tau_d$(Chl). There is a threefold variability in τ_d for SST and Chl even within regions that are traditionally considered to be biogeographically homogeneous. The largest τ_d for Chl is generally found on the equatorial side of the trade wind belts, whereas the smallest τ_d are found in the tropical Pacific and near coasts, especially where upwelling is common. If the temporal variability in Chl and SST were driven largely by ocean dynamics or advection by the flow, regional patterns of τ_d for SST and Chl should co-vary. This is seen in coastal upwelling zones, but more broadly, the lack of coherence between τ_d(Chl) and τ_d(SST) suggests that biological processes, such as phytoplankton growth and loss, decouple the timescales of Chl variability from those of SST and generate shorter term variability in Chl.

1. Introduction

In many regions of the ocean, primary production is punctuated by hotspots (Oliver et al., 2021) and blooms (Alkire et al., 2012) that exhibit high spatial and temporal variability in phytoplankton biomass (Zingone et al., 2010). A classic example of how periodic changes in primary production have profound effects on the food web and export of carbon is the annual North Atlantic spring bloom (Sverdrup, 1953; Sundby et al., 2016; Briggs et al., 2011; Behrenfeld and Boss, 2017; Henson et al., 2009; Stramska and Dickey, 1993; Platt et al., 2003; Martin et al., 2011). The suggestion that temporal changes in phytoplankton biomass might be as important as the mean standing stock has lead to increased interest in how best to evaluate the variability of phytoplankton over different temporal and spatial scales. Variability has been investigated on daily (Abbott and Letelier, 1998), intra-annual (Legaard and Thomas, 2007), annual (Dunstan et al., 2018), and inter-annual timescales (Henson et al., 2009), as well as on sub-kilometer spatial scales (Blackwell et al., 2008). Reviews by McClain (2009) and Mahadevan (2016) discuss how interactions between biological and physical processes occur on different temporal and spatial scales.

Satellite-derived proxies for biomass such as Chlorophyll (Chl) and Particulate Organic Carbon (POC) are now available at unprecedented coverage in time and space, enabling better estimates of the variability in biomass of phytoplankton and of total organic particulates on different scales (McClain, 2009; Siegel et al., 2013). However, one key challenge when working with satellite-derived products is data gaps

Abbreviations: MOSS, MOving Standard deviation Saturation; SST, Sea Surface Temperature; Chl, Chlorophyll; OC-CCI, Ocean Colour Climate Change Initiative; SST-CCI, Sea Surface Temperature Climate Change Initiative.

* Corresponding author.
E-mail address: brj@pml.ac.uk (B.F. Jönsson).

https://doi.org/10.1016/j.rse.2022.113404
Received 19 June 2022; Received in revised form 28 October 2022; Accepted 30 November 2022
Available online 23 December 2022

caused by factors such as clouds, sun angle, and sun glint, all of which obfuscate the satellite sensor's view of the ocean. These erroneous data acquired under these adverse conditions, usually flagged for removal, are not evenly distributed, but follow patchy irregular patterns determined by the temporal and spatial scales of synoptic weather systems or seasonal variability in the conditions (for example in the sun angle) in different regions. Consequently, only 20% of the derived Chl fields are on average useful (Fig. 3) (Lee et al., 2012). Such sparse and unevenly distributed datasets create a major challenge for common timeseries analysis tools, such as Fourier analysis or Empirical Orthogonal Functions (EOFs), thus hindering efforts to understand the frequency distribution of the data. A common and very successful approach is to aggregate the daily satellite fields to monthly averages to obtain full or almost full spatial coverage (Henson et al., 2009; Yoder and Kennelly, 2003; Glover et al., 2018). The resulting analyses provide spatial distributions and insight about changes in phytoplankton biomass on seasonal or longer timescales, but truncate high-frequency variability that may occur on timescales less than a month. Reviews by Blondeau-Patissier et al. (2014) and Zingone et al. (2010) provide a comprehensive overview of statistical analyses used in time series analyses of phytoplankton biomass.

To better meet these specific challenges associated with time series analysis of sparse satellite derived properties, we suggest a new method to estimate dominant timescales of variability (τ_d) that can detect the effect of processes with higher frequencies than earlier methods. The dominant time scale τ_d is a quantity that scales with the point along the frequency domain where 50 percent of the variability in a given time series is accounted for. The approach is similar to semi-variograms (Journel and Huijbregts, 1978; Doney et al., 2003; Glover et al., 2018) and the analysis of spatial patchiness described in Mahadevan and Campbell (2002), but describes temporal variability rather than the spatial autocorrelation or patchiness in the satellite field. An application of moving standard deviations with varying window sizes, but to estimate the amplitude of short-term fluctuations over a diurnal cycle, is presented in Hocke et al. (2019). A separation into sub-seasonal, seasonal and interannual time scales is performed by Keerthi et al. (2020); Prend et al., 2022 for the Mediterranean Sea and Southern Ocean.

The technique is based on calculating the standard deviation (σ) of the time series data over moving windows of a set time interval, and repeating for different time-interval windows. The average σ for each time-window size ($\overline{\sigma}$) increases from zero for a time window that includes just one data point, to σ of the full time series. The largest possible time window is in effect the full time series. The shape of the resulting curve of $\overline{\sigma}$ vs. the time-interval window size (w) is then analyzed to identify a dominant timescale, τ_d, of the time series for every pixel (or location). The method is developed to have specific skill in identifying time series where short time scales dominates over long-term, normally seasonal, variability. It should be noted that any noise in the time series has a first order effect on the estimated dominating timescale. This is a desirable feature since noise adds to the variability and should be accounted for. The method does not try to identify specific signals or periodicities in the data, but the timescale of variability that is most important.

First, we present our proposed method of analyzing satellite time series to identify the dominant timescale of variability, τ_d. We then apply the method globally to satellite derived Chl and Sea Surface Temperature (SST) data to analyze significant differences in timescale variability of Chl and SST, as well large regional patterns in Chl and SST variability. Finally, we discuss how results relate to known physical drivers of phytoplankton production in different regions of the global oceans.

2. Methods

2.1. MOving Standard deviation Saturation (MOSS)

The *MOSS* method is based on the concept that a small section of a time series only includes variability on timescales smaller or equal to the size of that section, while variance on longer timescales is invisible. Larger sections will include more variability, with standard deviation increasing to the point where all variance in the time series has been accounted for. By defining a window of a specified length (w) and calculating the mean of the moving standard deviation over the time series ($\overline{\sigma}(w)$), one can estimate how much variability on timescales less than or equal to w contributes to the total variance. The $\overline{\sigma}$ calculation can be performed using any size of w up to the length of the full time series, where the result will by definition be the standard definition of the full time series. The $\overline{\sigma}$ can rapidly reach σ of the full time series with a smaller w if the variability is primarily concentrated at smaller timescales.

The MOSS method expands on this notion by calculating $\overline{\sigma}$'s using varying w, starting at one day and increasing the window size stepwise. We limit the analysis to $w = 400$ days to avoid inter-annual variability that might dominate results. Variability in Chl and phytoplankton biomass on interannual to decadal timescales has been thoroughly discussed in earlier studies (e.g. Henson et al., 2009) and the purpose of this study is to investigate variability over shorter timescales that have received less attention. The resulting curve of $\overline{\sigma}$ will start at 0 for a window length of one and saturate at σ of the full time series (denoted as σ_{max}). We interpret the slope of the curve as reflecting how fast the variability included in windows smaller than or equal to a specific w converges to the total variability, thus providing information about timescales that most capture variability in the full time series. A steep slope shows that small window sizes can capture most of σ_{max} and suggest a time series dominated by short timescales. A more gradual slope is indicative of long timescales being dominant and/or the presence of pronounced temporal autocorrelation which would act as a low-pass filter. The steepness of the slope can then be used as a proxy for which timescales are contributing most to the variability in the time series. Different methods to estimate the slope is discussed in the Results section.

2.2. Satellite data

Analyses are based on daily satellite-derived fields of Chl and SST with a 4 km resolution for the period 2006–01-01 to 2016–12-31. Chl is sourced from version 4.2 of Ocean Colour Climate Change Initiative (Mélin et al., 2017; Sathyendranath et al., Oct. 2019, 2020, OC–CCI), which is a level 4 blended product. OC–CCI V4.2 merges data from the Sea-viewing Wide-Field-of-view Sensor (SeaWiFS), the Aqua MOderate-resolution Imaging Spectroradiometer (MODIS-Aqua), the MEdium spectral Resolution Imaging Spectrometer (MERIS), and the Suomo-NPP Visible Infrared Imaging Radiometer Suite (NPP-VIIRS) into a unified product. SeaWiFS operated from September 1997 until December 2010, MERIS from March 2002 to May 2012, while MODIS-Aqua was launched in May 2002 and VIIRS in October 2011; the last two are still operational as of December 2021. Data from the different instruments are merged after band-shifting normalized remote-sensing reflectance (R_{rs}) to the spectral bands of SeaWIFS and correcting for inter-sensor biases. Atmospheric correction is performed using POLYMER v3.5 (Steinmetz et al., 2011) for MERIS and MODIS-A, and NASA/L2Gen 7.3 for SeaWiFS and VIIRS. All individual grid cells are classified optically using a fuzzy-logic clustering approach (Moore et al., 2009; Moore et al., 2012; Jackson et al., 2017) and a combination of the best performing Chl algorithms for each class is employed along with membership information for each pixel at each time to calculate the best estimate of Chl. The spatial mapping follows NASA protocol for level 3 processing by considering a 4-km bin as valid if there is at least a single 1-km valid pixel from at least one sensor, and taking the average if more than one value is valid. The resulting time series is designed to be internally consistent (all radiometric products band-shifted to a common set of bands corresponding to SeaWiFS) and stable (corrected for inter-sensor bias), thus providing a more extensive temporal coverage than any

individual instrument.

SST is based on the ESA SST CCI Analysis Long Term Product (Merchant et al., 2019; Merchant et al., 2016; Good et al., 2019, SST-CCI), consisting of daily, spatially complete fields obtained by combining the data from the AVHRR and Along Track Scanning Radiometer (ATSR). Gaps are filled using optimal interpolation and other data assimilation methods to provide SSTs where there were no measurements (Merchant et al., 2019). SST-CCI provides a representative SST at the foundation depth, defined as the starting point of the diurnal cycle that will develop over a day, i.e. at 20 cm depth at 10:30 in the morning local time. The mean density of good-quality observations is 13 km^{-2} yr^{-1} (Merchant et al., 2019). SST uncertainty is evaluated per datum, the median uncertainty for pixel SST being 0.18 K. Multi-annual observational stability relative to drifting buoy measurements is within 0.003 K yr^{-1} of zero with high confidence, despite maximal independence from in situ SSTs over the latter two decades of the record (Merchant et al., 2019). The data products from SST-CCI accurately map the surface temperature of the global oceans over the period 1981 to 2016 using observations from many satellites and provide independently quantified SSTs to a quality suitable for climate research. The SST-CCI product was natively developed on a 0.05° grid with full daily coverage. The daily fields are re-projected to the OC-CCI grid using the SatPy resampling package (Raspaud et al., 2019) and any pixels that are invalid in the OC-CCI dataset are masked out.

3. Results

We begin our analysis by applying the MOSS method to synthetic data as a means to explore how time series relate to different estimates of dominant timescales. Fig. 1 shows an example of a sinusoidal time series (upper panel) and MOSS calculated from $\overline{\sigma}$ with different window sizes (blue line, lower panel). The resulting MOSS curve is, as expected, monotonic and reaches σ_{max} when the window size is the same as the full period of the sine curve. The shape has superficially similar properties to a growth curve described by the Monod equation (Monod, 1949).

$$y = \frac{\sigma_{max} \cdot x}{B_0 + x} \tag{1}$$

which is specified by a half saturation constant (B_0) controlling the slope of the curve and σ_{max} analogous to maximum standard deviation. We test the similarity by applying a curve fit of Eq. (1) using the Levenberg–Marquardt algorithm, as implemented by the *scipy optimize* package (Virtanen et al., 2020) and find a reasonable similarity (red dashed lines in the lower panels of Fig. 1). The main difference is that the fitted Monod function reaches saturation much later than the MOSS curve. To address this lack of saturation by the Monod fit, we investigate a more simplistic approach by defining the half saturation constant (denoted as K_M) as w when $\overline{\sigma}$ is half of σ at $w = 400$.

While a sinusoidal curve is a reasonable model of the seasonal SST cycle, it is too simplistic a representation of the annual Chl cycle (Jönsson et al., 2013; Jönsson et al., 2015). A more realistic, albeit crude, synthetic time series is shown in Supplementary Fig. A.1, where the sinusoidal curve in Fig. 1, panel A has been truncated below 0.01. The premise of this form of seasonality is that phytoplankton communities are dormant during winter and Chl becomes negligible. We apply the MOSS analysis to the time series and find that while the amplitude of σ_{max} decreases, the slope of the curve and K_M are similar to the full sinusoidal signal. In the Monod fit B_0 increases by about 30 days. Fast Fourier Transform (FFT) for the truncated time series produces two significant peaks in the resulting spectrum: one at 187.5 days and another at 365 days. The MOSS approach is not sensitive to the the shape of the curve, as can be seen in Supplementary Figs. A.2–A.5 where triangle and sawtooth curves have been used instead of a sinusoid.

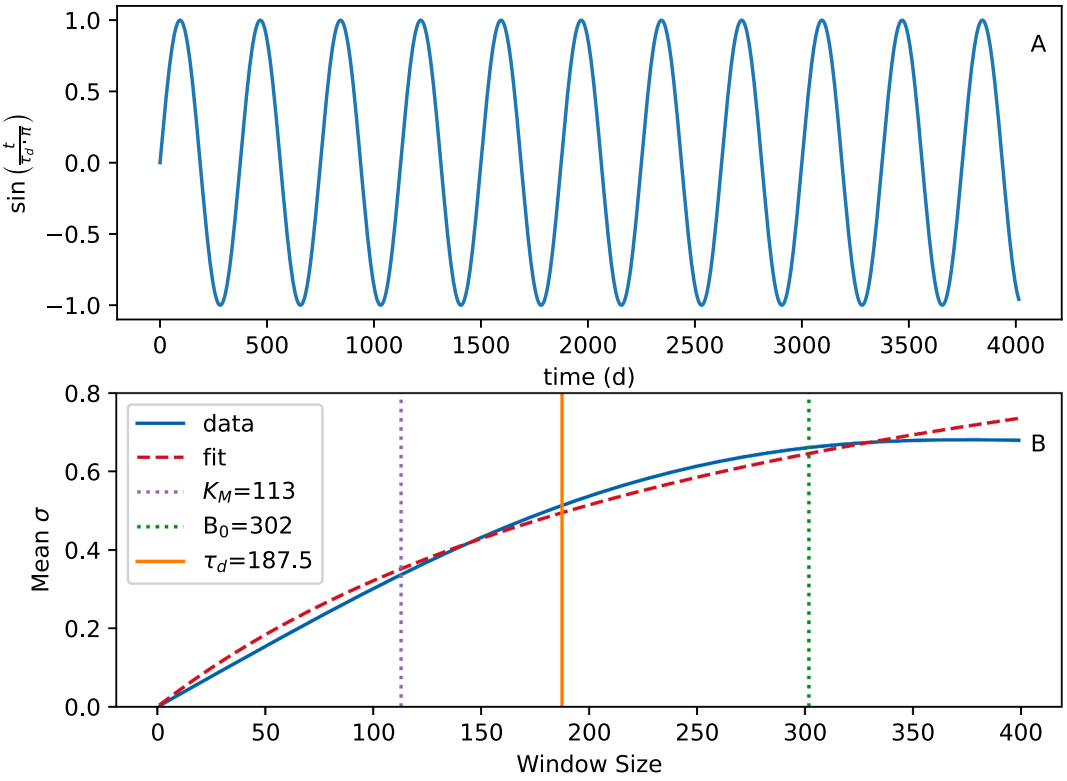

Fig. 1. Panel A: Time series constructed from a sinusoidal curve with a one year period. Panel B: Mean moving standard deviations (blue solid curve) calculated using the time series in panel A at different window sizes. The dashed red curve shows a curve-fit based on a Monod equation, green dotted line the half saturation constant (B_0) from the Monod equation, and the purple dotted line the half-saturation constant estimated directly from the blue curve (K_M). τ_d (orange solid line) depicts the dominant timescales as defined in Section 3.2.

3.1. Half saturation constants

These analyses show that both B_0 and K_M have utility in describing the slope of the MOSS curve in these idealized cases. K_M seems to be slightly more robust by providing the same value when comparing the two curves, which we would expect to have similar if not identical slopes. Since B_0 requires a computationally expensive optimization without providing any further advantages, we hereafter choose to use K_M to represent the slope of the MOSS curve for systematic comparisons between different time series.

3.2. Scaling the half saturation constant to dominant timescales

While the expression "seasonal timescales" is commonly used and intuitively understood, there is, to our knowledge, no formal definition of the term. Even the number of seasons varies from two to six depending on which world region is being discussed (Jefferson, 1938; Trenberth, 1983). To create a technical definition of seasonal timescales for the practical and illustrative purpose of exploring utility of the MOSS method, we expand on Trenberth (1983) and assume a simple seasonal cycle based on a delta function varying every six months which thus defines the timescale of variation as $\tau_d(season) \equiv 182.5$ days. The earlier described full and truncated sinusoidal time series (see Fig. 1) can be interpreted as different representations of a seasonal cycle with two seasons. We find that τ_d of 182.5 days (presented as a solid purple line) falls between the two half saturation constants. It is also one of the spectral peaks in the FFT of the truncated sinusoidal times series. The full sinusodial time series shown in Fig. 1 has a spectrum with only one peak, at the 365 day period.

Differences in the magnitude of K_M can be used to distinguish time series with varying dominating time scales, but the metric has in itself no direct physical meaning. To address this issue, we develop a simple scaling factor between K_M and τ_d. It is clear from the initial analysis that such a relationship is dependent on the number of values missing in the time series. Solid lines in Fig. 2 show the half saturation constant for a number of sinusoidal time series with different timescales and with different percentage of values missing. Each curve in the figure is based on a Monte-Carlo simulation where 1000 time series have been created but randomly replacing values with NaN's before calculating the half saturation constant with the MOSS method and averaging the calculated K_M for each C, where C is the coverage, defined as the percentage of valid values in the time series (i.e. a 10% coverage means that 90% of the values in the time series are invalid, or $C = 90\%$). See Fig. 3 for a global map of C for daily merged ocean-color data. For the Monte Carlo simulations, the resulting curves for different coverages show a linear relationship at longer timescales, but with different slopes and intercepts depending on C. We minimize these differences by applying the linear relationship $\tau_d = \beta_1 K_M + \beta_0$, where

$$\beta_1 = \frac{1.38}{C} + 1.62 \tag{2}$$

and

$$\beta_0 = 1.086 \cdot \left(1 - 50.4 \cdot e^{-0.092C}\right) + 0.14. \tag{3}$$

The influence of C on β_0 is described using a Weibull Continuous Distribution Function with a second exponent of 1 (Weibull, 1951). All parameters are estimated using the Levenberg–Marquardt algorithm, as implemented by the *scipy optimize* package (Virtanen et al., 2020). Data used for curve fits are shown together with the resulting relationships in Figs. A.7 and A.8 in the Appendix. Please note that K_M and τ_d are switched in Fig. 2. Dotted lines in Fig. 2 show the result of scaling K_M (solid curves) to τ_d using β_1 and β_0 from Eqs. (2) and (3). MOSS shows good skill in estimating τ_d longer than 10 days when the coverage is better than 10%. We use these values as the cutoff under which data are discarded (as shown in Fig. 3).

3.3. Examples of daily satellite-derived time series

As a next step, we calculate K_M, and τ_d based on the MOSS curves constructed from daily time series of Chl and SST from the OC-CCI and SST-CCI satellite-derived products. Fig. 4 shows time series, MOSS curves, K_M, and τ_d for for seven individual locations in the Pacific Ocean along the 159.15°W meridian at different latitudes (locations marked on Fig. 3). All locations are chosen to have a daily coverage of at least 15% and represent regions with significantly different physical, chemical, and biological conditions. Locations in temperate and subtropical regions (panels A, B, F, G) show a pronounced seasonal sinusoidal cycle with relatively low intra-seasonal variability. For these sites, τ_d is close to 180 days. τ_d for SST in panel A is longer than 6 months, which should not be possible and is primarily caused by seasonal aliasing due to long periods of invalid values caused by low solar angles during the polar winter (Jönsson et al., 2020). The SST-CCI product is by itself not affected by low solar angles but uses the same mask of invalid values as the OC-CCI Chl product. The sinusoidal seasonal SST cycle is lagged compared to the astronomical year so that the coldest period occurs several months later than the period with the lowest light. This offset creates a spurious step function where the last observed fall temperate data point is significantly higher than the first value recorded the next season. The resulting discontinuity leads to an overestimate of τ_d from MOSS when a moving window larger than the seasonal scale bridges the winter gap and includes both fall and spring values.

The Chl time series in Panels A, B, E, and G show a similar, albeit much less pronounced, seasonal variability as the SST time series in the temperate and subtropical regions. The higher variability over short timescales in combination with a lack of a sinusoidal structure in the

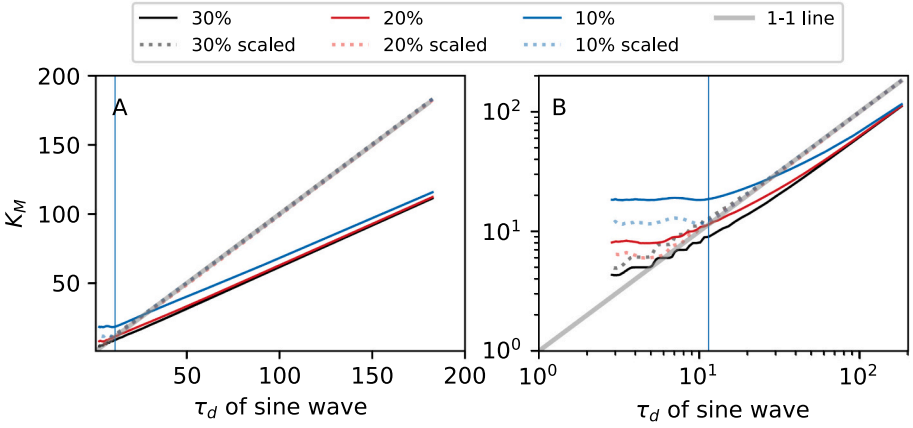

Fig. 2. Panel A: Relationships between τ_d and K_M for sine waves with different wavelengths and coverage of valid data points (solid lines), and linearly scaled using a coverage dependent equation for the slope and intercept (dotted lines). Higher coverages are identical to the 30% lines and omitted. For a sine wave, τ_d is defined as half of the period, as discussed in Section 3.2. Panel B is identical to panel A but with axes on a log–log scale. Please note that the linear regression was performed with K_M as independent and τ_d as dependent variables. The vertical lines represent the inflection point.

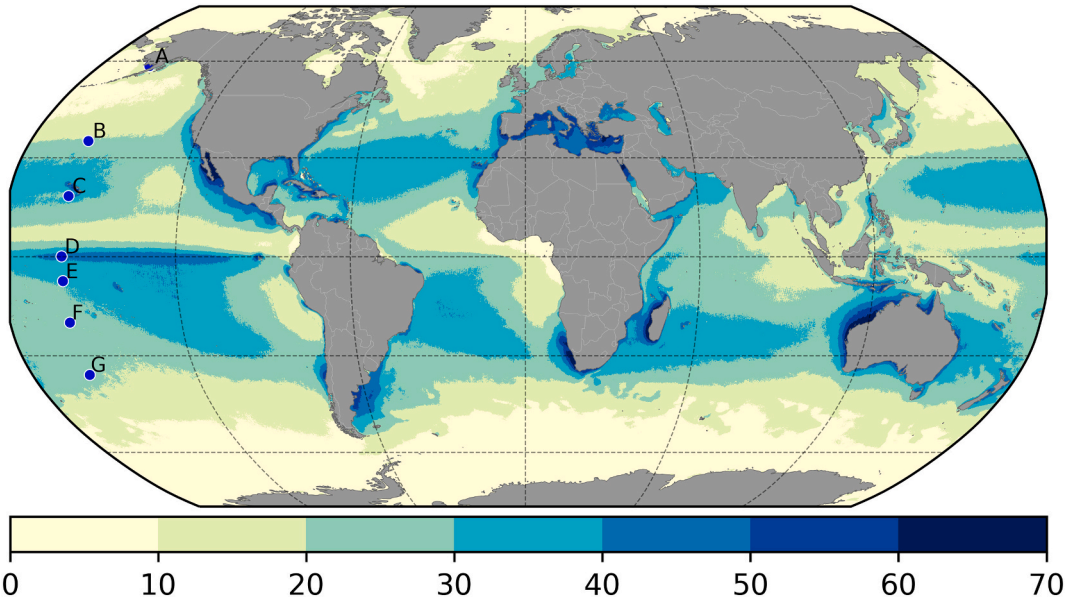

Fig. 3. Temporal coverage (in percent) of daily data in Ocean Colour Climate Change Initiative (OC-CCI) and Sea Surface Temprature Climate Change Initiative (SST-CCI) for the period 2006–01-01 to 2016–12-31. Blue dots denote locations of the time series in Fig. 4. Labels A-G here correspond to the panels in Fig. 4.

seasonal variability leads to significantly shorter τ_d than for SST. A notable exception is panel B (35°N), where Chl and SST seem to show similar behaviors. Closer examination indicates, however, that Chl has more high frequency variability in seasons with low Chl and hence shorter τ_d. The Chl time series in panel G includes an episodic event with very high Chl during the growing season. This spike is interpreted as variability on short timescales by MOSS and the τ_d is shorter as a result.

SST in the tropical regions (panels C-E) exhibits less regular seasonal patterns and larger inter-annual variability. MOSS is still able to characterize the variability and the resulting τ_d are only slightly shorter than for the subtropical and temperate regions. Chl exhibits mainly stochastic patterns interrupted by episodic events, resulting in much shorter τ_d.

3.4. Meridional segment

All examples in the last section are located along the same meridian in the central Pacific Ocean, at 159.15°W. We extend our analysis by calculating K_M and τ_d for all grid cells along the line, as shown in Fig. 5. Data based on the SST-CCI time series (left panel) show a consistent global pattern with long τ_d at high latitudes that gradually decreases towards the equator. The intertropical convergence zone is clearly visible with small regions of longer τ_d, probably due to seasonal oscillation where the Hadley cell terminates. The local minima at about 20°N, associated with a local maxima in coverage, is connected to local processes around the Hawaiian islands (as seen more clearly in Fig. 6). This tendency to shorter τ_d in coastal regions with be discussed in more detail later. The drop in τ_d between 40 and 60°N is also connected to coastal conditions. It should be noted that coverages below 10% of valid datapoints in individual time series at high latitudes limits the ability for MOSS to consistently identify τ_d.

The τ_d calculated from OC-CCI time series (Fig. 5, panel B) show a very different global pattern than the ones based on SST-CCI. The values are, with some exceptions, generally lower for OC-CCI and without a pronounced gradient from high to low latitudes. Instead, we see local minima at 20°S, the equator, and 20°N, and local maxima just north of 40°S, 10°S, 10°N, and just south of 40°N. We will discuss these patterns and their global occurrence consistency in more detail next.

3.5. Global patterns

We expand our analysis to include the full global domain of OC-CCI and SST-CCI. Fig. 3 shows the global relative coverage of Chl and SST based on daily time series for each individual pixel in the grid. OC-CCI and SST-CCI has the same coverage in this analysis since a mask with invalid values in OC-CCI has been applied to the SST-CCI dataset. Most areas in the ocean fulfill the condition of at least 10% valid pixels for MOSS to provide reasonable results. Coverage falls below this threshold in polar regions where low sun angles and lack of daylight during the winter season limits detection (Jönsson et al., 2020) and in tropical regions with extensive cloud cover. The coverage by OC-CCI is significantly better than what is possible to attain with a single sensor such as MODIS-Aqua, as seen in Supplementary Fig. A.6. This is due to a combination of OC-CCI blending data from different instruments to a Level 4 product and the use of improved atmospheric correction methods (Steinmetz et al., 2011).

The analysis along a single meridian described in Section 3.4 is expanded by applying MOSS to the daily time series at all pixels in the global domain. The global distributions of K_M and τ_d for SST-CCI and OC-CCI are shown in Figs. 6 and 7, respectively. We find that the meridional distribution shown in Fig. 5, panel A for SST-CCI is representative of the global patterns of K_M and τ_d. Largest values are found at high latitudes while gradually getting smaller towards the equator. Some notable exceptions are the California, Humboldt, Benguela and Canaries Eastern boundary upwelling systems together with smaller regions such as the Galician coast. Highly energetic areas such as western-boundary currents and the Antarctic Circumpolar Current (ACC) have smaller τ_d than surrounding areas at the same latitude. The short τ_d North of the ACC and South-South-East of Africa is somewhat non-intuitive and is suggestive of sub-meso- and mesoscale processes dominating the system, something that has been discussed in earlier studies. The Amazon river plume is also visible as having shorter timescales than the surrounding region. The largest area with very short dominant SST-CCI timescales are found in the coral triangle, possibly resulting from strong variability in surface currents and low seasonal variability in SST.

K_M and τ_d calculated from OC-CCI (Fig. 5, right panel) show a very different global pattern than results based on SST-CCI. With some exceptions, values are lower for OC-CCI and without a pronounced

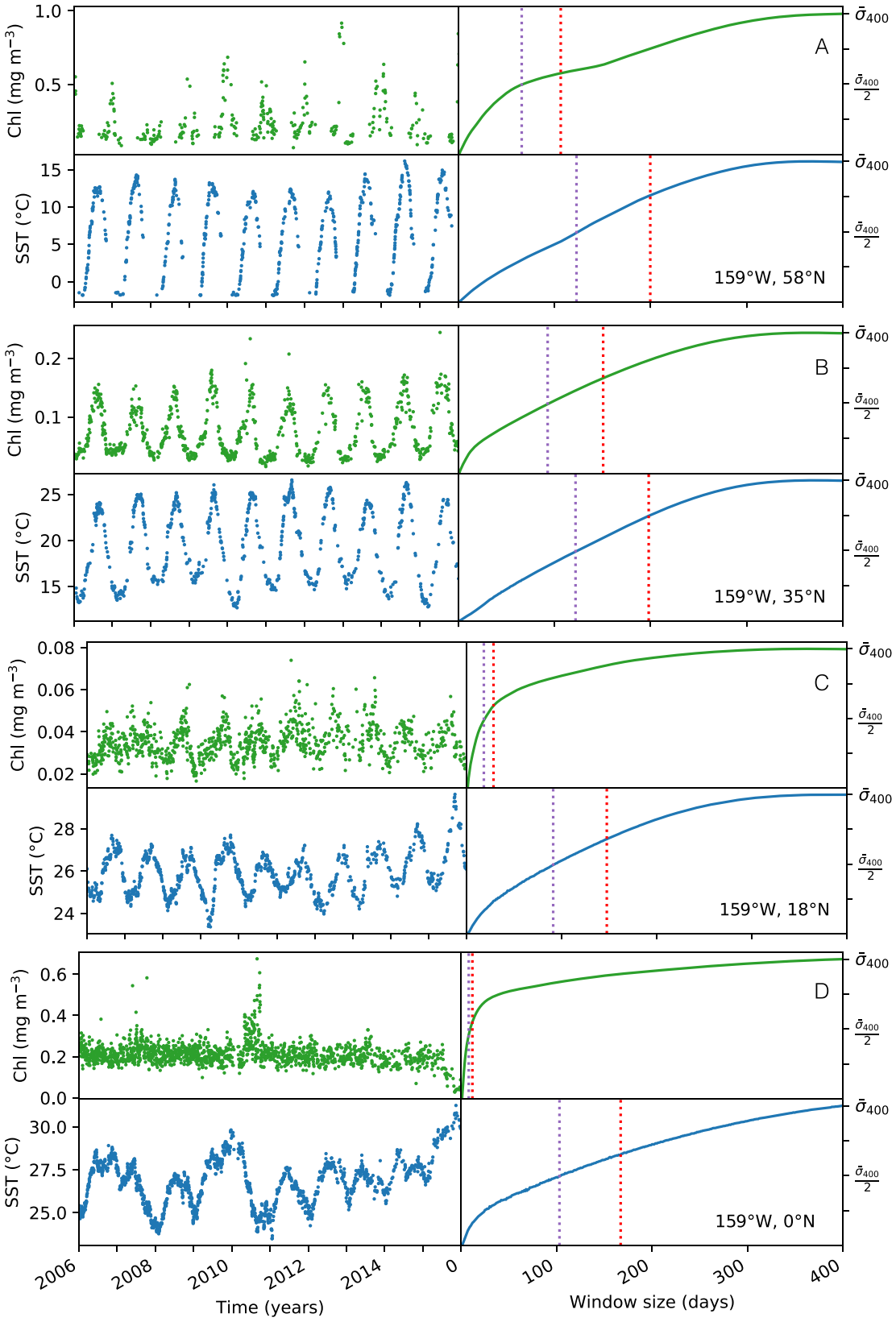

Fig. 4. Examples of time series (left panels) and MOSS curves (right panels) for Chl (green) and SST (blue) from grid cells along the 159°W meridian in the Pacific. Purple dotted lines denote K_M and orange dotted lines τ_d. $\overline{\sigma}_{400}$ denotes $\overline{\sigma}$ when the window size is 400, which is used to calculate K_M. The location of each time series is shown in Fig. 3.

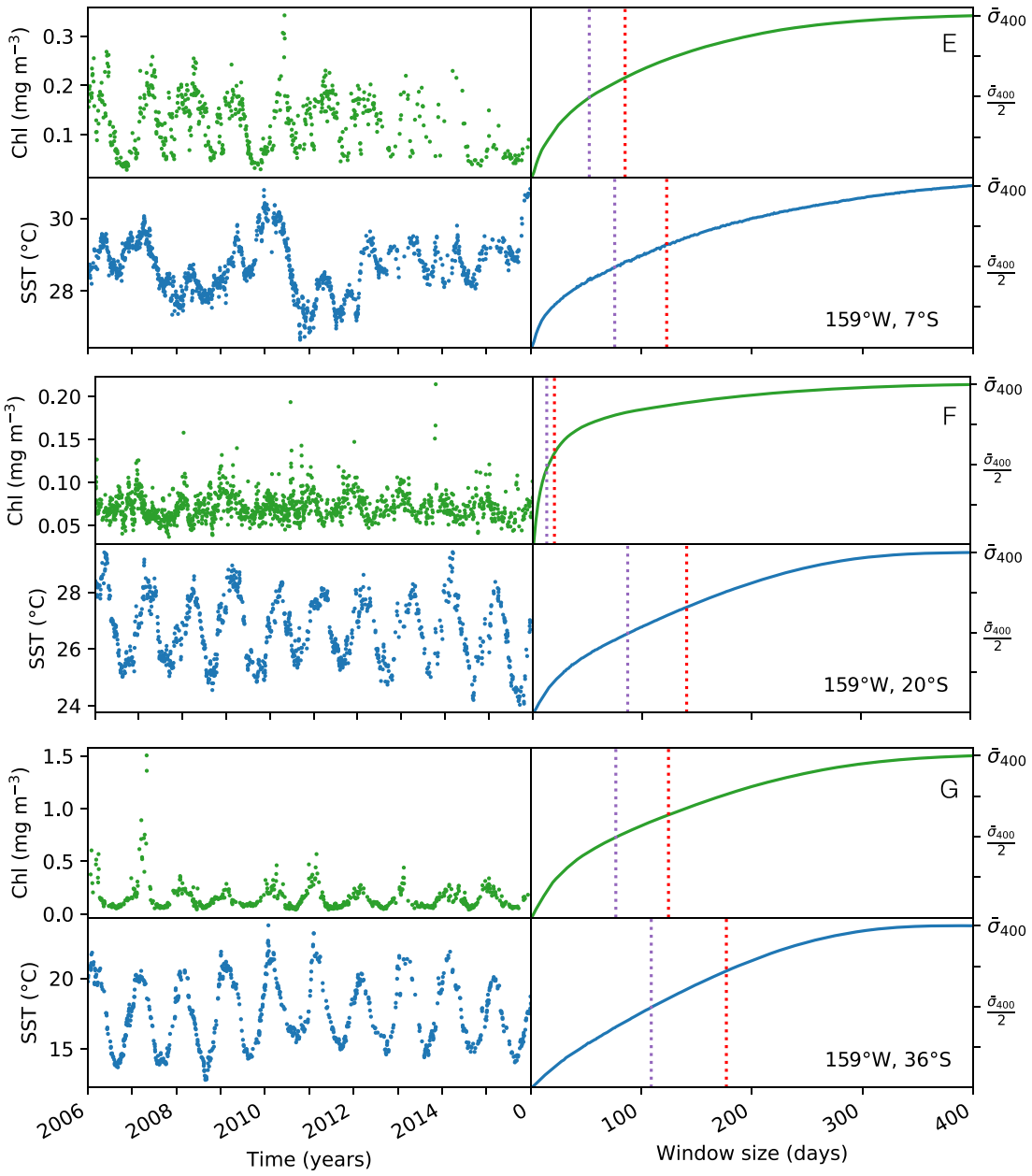

Fig. 4. (*continued*).

gradient from high to low latitudes. Longest τ_d for Chl are generally found on the equatorial side of the trade wind belts, whereas lowest values can be found in the tropical Pacific and near coasts, especially where upwelling is common. We see areas with longer timescales on the west coast of Panama and in the Arabian Sea that seem to coincide with persistent wind patterns. In comparison to the earlier discussed longer timescales of SST in temperate regions, there is no clear seasonal signal from the North Atlantic spring bloom in the Chl data and a clear albeit less pronounced signal that follows the Gulf Stream in both K_M and τ_d. The prominent bands with long τ_d visible just north of the Southern Ocean are possibly due to the seasonal progression of the boundary between oligotrophic waters in the gyres and surrounding areas with higher phytoplankton biomass.

It is clear that the subtropical and tropical patterns seen in the OC-CCI dataset at the 159.15°W meridian (Fig. 5, local minima at 20°S, 0°, and 20°N) are connected regional areas with very short τ_d, and not zonally representative. The local maxima just north of 40°S and just south of 40°N) in Fig. 5, panel B are associated to regions with long timescales seen in all oceans basins at similar latitudes.

3.6. Regional maps

MOSS not only identifies global patterns of τ_d but also has the potential to resolve structures on small spatial scales since each pixel in the OC-CCI grid is treated individually. It should be noted that since SST-CCI is upscaled to the OC-CCI grid, there is some spatial autocorrelation and the SST data should be interpreted with caution on very small scales. Fig. 8 shows detailed maps of five different regions of the ocean. All regions show coherent and realistic structures of long and short τ_d, strongly suggesting that the results are based on real features and not

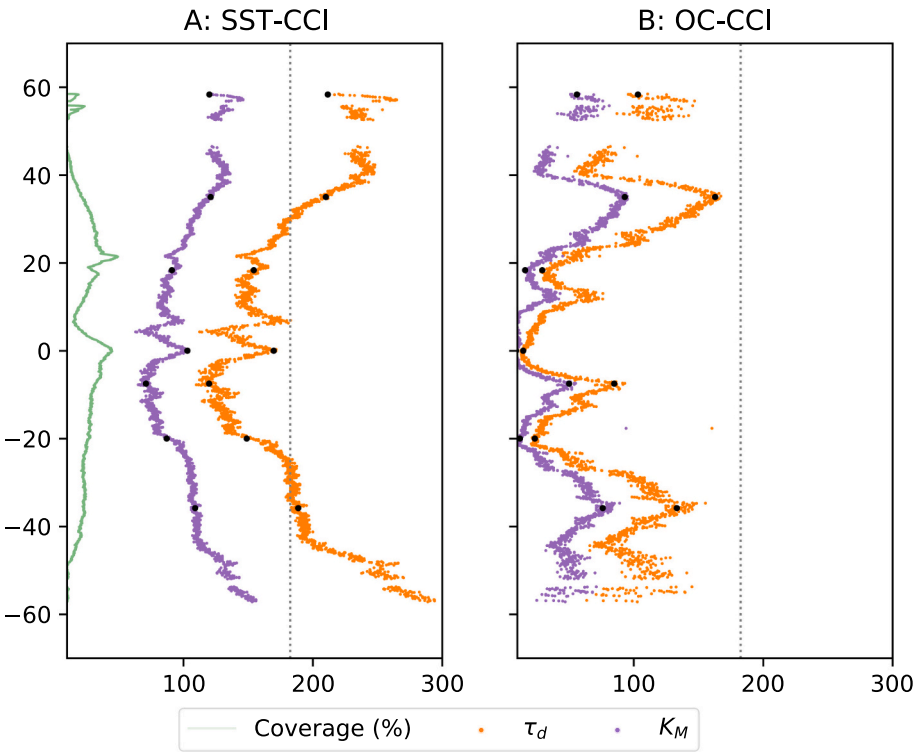

Fig. 5. Temporal coverage (green line, unit in percent), K_M (purple line, unit in window size), and τ_d (orange line, unit in days) along a meridian at 159.15°W for Sea Surface Temperature Climate Change Initiative (SST-CCI) (panel A) and Ocean Colour Climate Change Initiative (OC-CCI) (panel B). The coverage is identical for both products and has been omitted in panel B for clarity. The dotted line depicts an annual timescale of 182.5 days. Black dots denote the location of the time series shown in Fig. 4.

spurious artifacts from MOSS. The earlier discussed patterns with very short τ_d in Chl near coasts, especially in upwelling regions, are even clearer in the regional maps. These coastal features exists for SST as well, just less pronounced.

Each region has its own unique structures driven by local processes and conditions. The Caribbean, Gulf of Mexico, and Central American west coast (Fig. 8, panels A-B) generally show short timescales for OC-CCI, especially near the coast, possible due to advection of water masses with radically different Chl concentrations. Waters outside the west coast of Colombia have seasonal timescales, probably connected to monsoon driven processes. SST-CCI is significantly different, with two distinct upwelling cells on the west coast of Mexico and Guatemala, and generally longer timescales in the Caribbean. The patch of longer OC-CCI seasonal timescales in the Eastern Pacific discussed above occur in the SST-CCI data as well, together with a second center further offshore.

The northern Indian Ocean (Fig. 8, panels C-D) have generally τ_d on the order of two months for Chl, with some notable exceptions. The coasts of Pakistan, India, Bangladesh, Myanmar, and easternmost Oman generally have very short timescales. There is no direct indication of the Ganges river plume, suggesting that processes connected to seasonal variability in water discharges do not significantly control biological production in the area. We find four distinct cells of longer Chl timescales in the region, three coastal and one on the western side of the Maldives. SST have generally longer timescales and a more even pattern. SST generally has longer timescales and a more even pattern. It is possible to identify the Ganges river plume as a region with longer timescales, due to the strong seasonality in freshwater discharge (Durand et al., 2011). Other regions with strong seasonality are the Persian Gulf and Arabian Sea. One interesting domain is the central southern-most region, where we observe shorter timescales than the surrounding areas. This is peculiar since this is a region that should be strongly influenced by Monsoon dynamics and thus rather seasonal timescales.

Chl in the Northwestern Pacific Ocean (Fig. 8, panels E-F, which is the domain of the Geostationary Ocean Color Imager) show similar patterns to earlier discussed regions, with shorter timescales near the coast and intermediate values in the middle of the basins. Coastal areas don't have as short timescales as the earlier discussed regions and there is a large cell of long timescales in the south-eastern part of the domain. SST generally have seasonal timescales with the exception of the coast of Taiwan, eastern Korea, northern China, and eastern Japan. The latter is probably connected to the Kuroshio current.

The Northeastern Pacific (Fig. 8, panels E-F) shows expected patterns, with distinct upwelling areas along the US West Coast being distinguishable in both products. Chl shows shorter timescales than SST, in contrast to patterns along the West Coast of Mexico and Guatemala discussed earlier. Shorter timescales in variability of Chl in this upwelling area, as compared to SST, is supported by long time series data from the Monterey Bay Aquarium Research Institute. A shift in τ_d from longer to shorter timescales moving South to North past Point Conception is reasonable, in particular the closer to seasonal timescales in SST along the Southern California coastline considering the substantial shift between summer and winter temperatures for that region. Both Chl and SST have significantly shorter τ_d around the Hawaii islands (lower left corner), corresponding to where the North Pacific Subtropical Convergence Zone shifts position on a seasonal basis, but this effect is much more prevalent in Chl.

Chl in the Gulf of Maine (Fig. 8, panels I-J) have generally short τ_d with distinct cells of especially short values. This temperate region has no indications of seasonality in Chl, with the exception of individual pixels very close to the shore. It is not clear if these results are due to artifacts in the MOSS method or the processing workflow for satellite-derived data, thus is something that deserve further examination. The region around Cape Cod and Marta's Vineyard also show high variability in τ_d on very small spatial scales. These structures, however, look coherent and could suggest complex patterns in bio-physical couplings in the area. SST show a more expected pattern, with dominant timescales largely following seasonal variability. This result is to be expected since summer and winter water temperatures are dramatically different in the region. The main exception is an area of shorter τ_d in the lower right corner of the panel, most likely connected to the Gulf Stream. This region also show the longest τ_d for Chl.

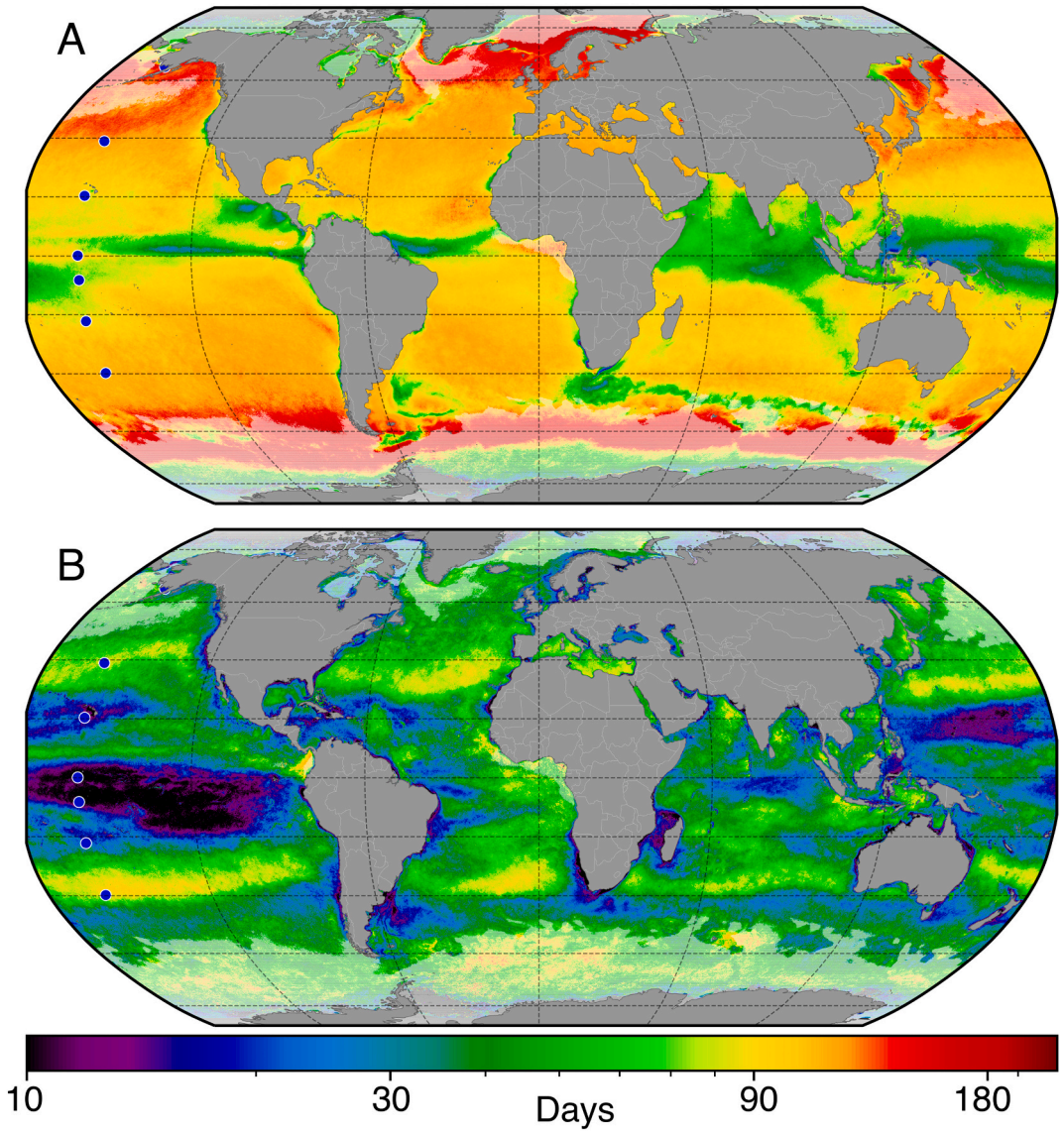

Fig. 6. Half saturation constant, K_M, of Sea Surface Temperature Climate Change Initiative (SST-CCI, panel A) and Ocean Colour Climate Change Initiative (OC-CCI, panel B) from the MOSS analysis for each grid cell using time series between 2006–01-01 to 2016–12-31. Regions with a temporal coverage of less than 10 % are shaded. Blue dots denote locations of the time series shown in Fig. 4.

4. Discussion

Our results show that the MOSS method has the ability to assess τ_d in time series where data coverage is sparse. Analysis of synthetic data sets suggests a threshold where estimated timescales start to diverge from actual ones is at about 10% coverage. The main consequences of sparse data is overly gentle sloping MOSS curves, which would exaggerate the dominant timescales. We compensate for this problem by scaling all K_M differently for different coverage in the original data sets. The scaling further allows us to interpret the resulting values as timescales of variability.

The MOSS method is able to detect dominant timescales longer than three days when the data coverage is higher than 30% and ten days where the coverage is between 10% and 30%. We don't recommend using the method where coverage is lower than 10% since the skill for detection below this threshold rapidly decreases, introducing a significant risk for spurious results. Most regions in the ocean have sufficient coverage above this threshold for the MOSS method to provide stable timescale estimates. This limitation is mostly of concern in high-latitude regions where winter light conditions restrict the retrieval of Chl observations. The seasonal cycle in Polar regions lead to confounding effects where the ecosystem in itself are affected by the same forcing that that can generate biases in Chl observations and statistical methods (see a more detailed discussion in Jönsson et al., 2020).

The ability by MOSS to detect timescales of variability down to the order of days is a significant improvement over methods such as Fourier analysis or Empirical Orthogonal Functions (EOFs), where the requirement of continuous time series is normally fulfilled by aggregating daily satellite fields to monthly averages (e.g. Henson et al., 2009; Yoder and Kennelly, 2003; Glover et al., 2018). Using the data presented in Fig. 7, we find that about 9% of the global ocean's area have Chl τ_d values below 30 days. Regions with Chl τ_d between 30–60 days occupy 23%, 60–90 days 28%, 90–120 days 21%, 120–150 days 12%, and regions with Chl τ_d longer than 150 days occupy about 7% of the global ocean. These results suggest the dominant timescales of variability for Chl can often be shorter than what earlier used methods were able to detect. The areal distribution of τ_d suggests that regions were Chl are varying on primarily seasonal scales are quite rare outside the polar regions. It is intuitive to believe that most regions where coverage is less than 10% have seasonal timescales for Chl τ_d, but this assumption remains to be

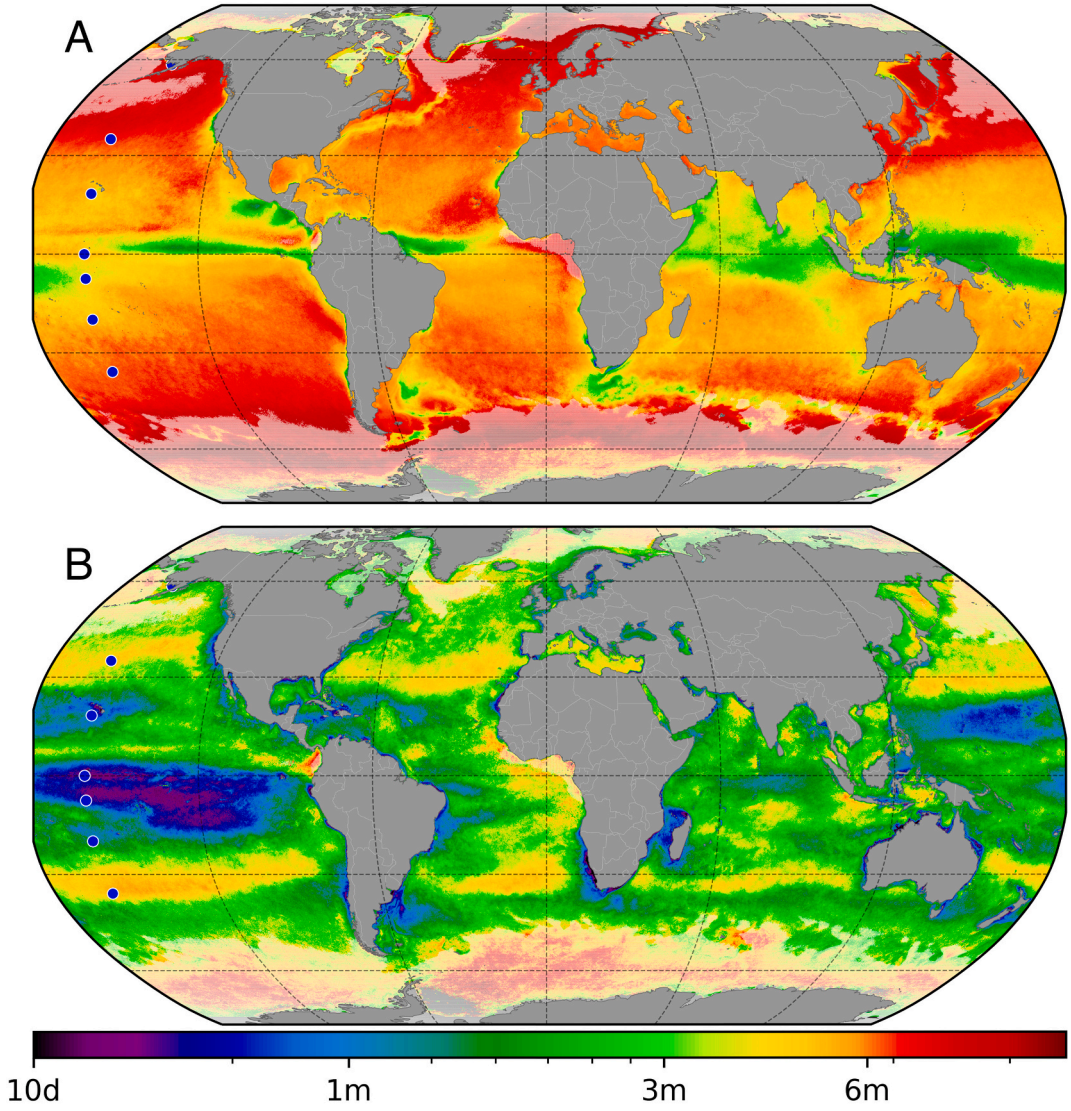

Fig. 7. Dominant timescales, τ_d, of Sea Surface Temperature Climate Change Initiative (SST-CCI, panel A) and Ocean Colour Climate Change Initiative (OC-CCI, panel B) for the period 2006–01-01 to 2016–12-31. Regions with a temporal coverage of less than 10 % are shaded. Blue dots denote the location of the time series shown in Fig. 4.

verified.

The global maps of τ_d provide new insights into the variability of SST-CCI and OC-CCI. The patterns are robust and have physical explanations, strongly suggesting that real-world processes are behind the observations rather than artifacts from the method. Regions that traditionally would be considered as homogenous according to biogeographical divisions, such as ecological provinces according to Longhurst (2007), can differ threefold in timescales. This could have profound effects on community composition of primary producers in the different regions - small organisms would benefit in regions with short dominant timescales since in general they can grow faster. This suggestion is supported by earlier studies reporting that dominant timescale of variability may be correlated with the composition of the marine microbial community (Berger and Wefer, Dec. 1990; Giovannoni et al., 2012). Variability in dominant timescales could hence help explain the variability in observed phytoplankton biodiversity in the world oceans. Furthermore, it is possible that zooplankton with different life strategies would be better adapted to specific timescales. The two main approaches could be either "winter" the variability in phytoplankton biomass or have the population increase and decrease with available food. The former could be a better strategy when short timescales are dominate, and the latter might be more successful for areas with longer timescales. These are put forward as speculations, but perhaps warrant further investigation. Another future use of the suggested framework to quantify dominant timescales would be to compare global biogeochemical models with observations to evaluate how well models resolve different physical and biological processes that affect the variability in phytoplankton biomass.

It is clear from our results that dominant timescales in OC-CCI and SST-CCI have very little cohesive or consistent correlation over large areas, and that SST generally displays longer τ_d than Chl. Patterns are geographically consistent and illustrative of well recognized regional processes. Chl data have shorter τ_d in temperate and polar regions, with the exception of some small areas close to the Antarctic and the Alaskan part of the Arctic Sea. These areas have very low coverage of valid data points and are possibly affected by regional ice coverage, both suggesting that the results can be spurious artifacts under conditions where the MOSS method is less reliable. In equatorial areas with more pronounced τ_d differences (eastern Pacific, Atlantic), coastal areas with with shorter Chl timescales are observed. The Amazon River plume is evident through less pronounced τ_d differences. The Gulf Stream is clearly detectable by having much smaller difference in τ_d than sur-

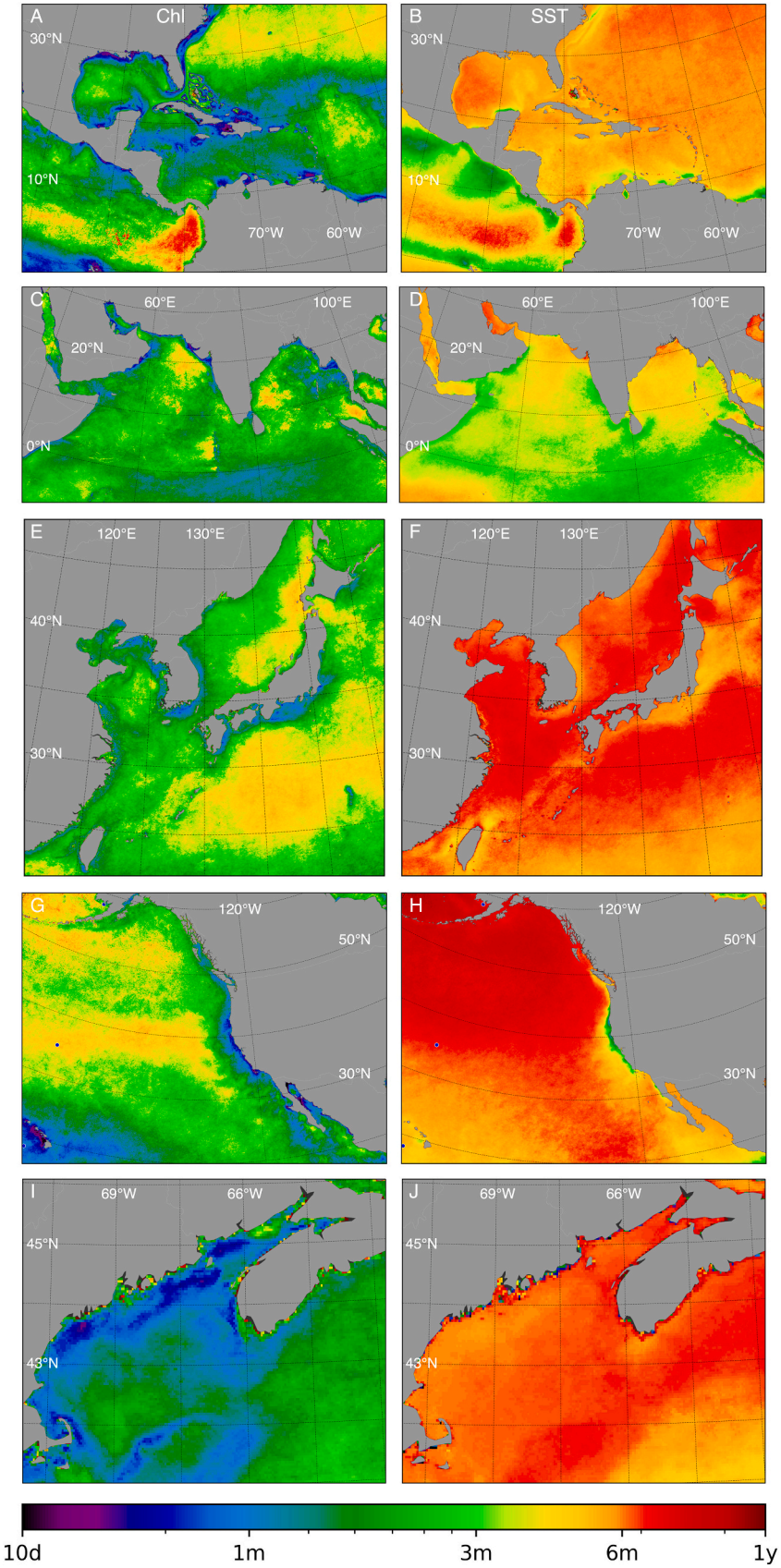

Fig. 8. Dominating timescales, τ_d, of Ocean Colour Climate Change Initiative (OC-CCI) and Sea Surface Temperature Climate Change Initiative (SST-CCI) in the Caribbean Sea (A-B), Indian Ocean (C-D), North-Eastern Pacific (E-F), North Western Pacific (G-H), and Gulf of Maine (I-J) for the period 2006–01-01 to 2016–12-31. Panels A,C,E,G, and I show Chl, and panels B,D,F,H, and J show SST.

rounding waters, a pattern also partially observed along the boundary with the Southern Ocean but that isn't detected for the Kuroshio current. The only regions in the lower latitudes where SST have shorter τ_d than Chl are some distinctive cells on the west coast of Colombia and Costa Rica, parts of the Amazon river plume, West of the Maldives, East of Sri Lanka, a region in the Arabian Sea, and East of the Coral Triangle. These areas are controlled by different physical, chemical, and biological processes with the only similarity being that they are located close to the equator. The disconnection between τ_d for Chl and SST suggests that biological processes are decoupled from those that control SST, generating shorter term variability in Chl. This potential decoupling should be investigated in the future.

Finally, we believe the MOSS method and τ_d estimates of dominant timescales of variability has a real potential to help constrain estimates of carbon export from the surface ocean to deeper waters. While the magnitude of export production and ecosystem efficiency is to a high degree based on physiochemical conditions and ecosystem composition, it has been suggested that the timescales of biomass change can play an important role (e.g. Brown et al., 2014; Buesseler, 1998). The hypothesis is that where ecosystems are characterized by gradual changes in autotrophic biomass, heterotrophs are able to utilize autotrophic carbon efficiently, resulting in tightly coupled food webs. Alternatively, systems dominated by shorter timescales or episodic growth tend to be more inefficient and likely to export a higher fraction of primary production (Brown et al., 2014; Buesseler, 1998; Longhurst et al., 1995; Dunne et al., 2007; Berger and Wefer, Dec. 1990; Fischer et al., Jan. 2000; Lutz et al., 2007; Henson et al., 2012). This idea is coherent with the finding in several studies that carbon export in itself an quite episodic with intense events occurring over short timescales (e.g. Muller-Karger et al., 2001; Scharek et al., 1999; Legendre, 1990; DiTullio et al., 2000). Together with earlier studies that have assessed the frequency of episodic events in biological production using satellite-derived products (e.g. Brown et al., 2014; Jönsson and Salisbury, 2016), our hope is that the method and results presented here can provide a framework for a concerted approach to connect the variability in biological production on different scales with export production and export efficiency.

5. Conclusions

We have present a novel method to estimate dominant timescales of variability: MOving Standard deviation Saturation (MOSS). The approach is similar to earlier analyses of spatial patchiness using semivariograms, but rather addresses temporal variability than spatial autocorrelation. We find that the method can assess dominant timescales in time series where data are very sparse. Analysis of synthetic data suggests a threshold at about 10% coverage. Our results reveal robust global and regional patterns which can be explained by physical or biological processes, but we find that regions traditionally considered to be biogeographically homogeneous can internally differ threefold in dominant timescales. Longest timescales for Chl are generally found on the equatorial side of the trade wind belts, whereas lowest values can be found in the tropical Pacific and near coasts, especially where upwelling systems are common. Dominant timescales in Chl and Sea Surface Temperature (SST) have very little cohesive or consistent correlation over large areas, with SST generally displaying longer timescales of variability than Chl.

These findings, while novel by themselves, have the potential to help explain patterns in observed global phytoplankton biodiversity; for instance, small organisms might have a competitive advantage in regions with short dominant timescales. Another potential use would be to constrain estimates of carbon export from the surface ocean for regions where it has been suggested that the timescales of biomass change may play an important role, together with physiochemical conditions and ecosystem composition. We believe that the MOSS method can provide a framework for a concerted approach to connect variability in phytoplankton biomass and biological production with export production and export efficiency.

CRediT authorship contribution statement

Bror F. Jönsson: Conceptualization, Methodology, Software, Validation, Formal analysis, Visualization, Writing - original draft, Writing - review & editing. **Joseph Salisbury:** Conceptualization, Methodology, Formal analysis. **Elizabeth C. Atwood:** Methodology, Validation, Formal analysis, Writing - review & editing. **Shubha Sathyendranath:** Funding acquisition, Writing - review & editing. **Amala Mahadevan:** Conceptualization, Formal analysis, Validation, Writing - review & editing.

Declaration of Competing Interest

The authors declare the following financial interests/personal relationships which may be considered as potential competing interests: Bror Jonsson reports financial support was provided by Simons Foundation. Bror Jonsson reports financial support was provided by NASA.

Data availability

Initial Data is available from NASA and PML. Results and code are available on request.

Acknowledgments

This work was carried out under the auspice of the Simons Collaboration on Computational Biogeochemical Modeling of Marine Ecosystems (CBIOMES), which seeks to develop and apply quantitative models of the structure and function of marine microbial communities at seasonal and basin scales. Data used in the study can be accessed athttps://doi.org/10.5285/D62F7F801CB54C749D20E736D4A1039F (OC-CCI) andhttps://doi.org/10.5285/62c0f97b1eac4e0197a674870afe1ee6 (SST-CCI). Funding for this work was provided by the Simons Foundation (549947 SS) and NASA (80NSSC21K0563, Lagrangian analyses of ocean color and 80LARC21DA002 – GLIMR). BJ and SS were part funded by ESA 4DATLANTIC Primary productivity in Upwelling Systems (PRIMUS). Additional support from the National Centre for Earth Observations of the UK is acknowledged.

Appendix A. Supplementary figures

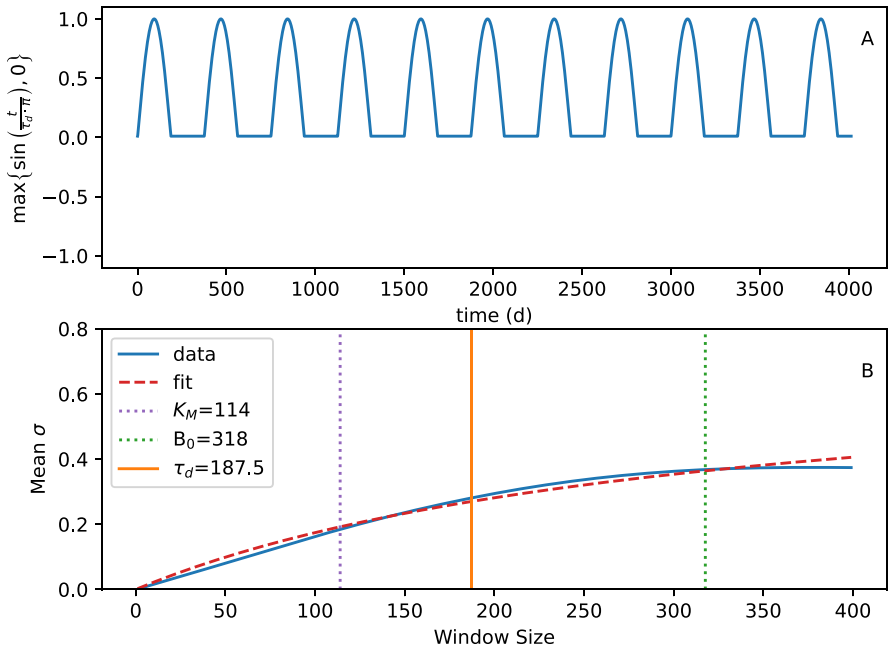

Fig. A.1. Panel A: Time series constructed from a truncated sinusoidal curve with a one year period. Panel B: Mean moving standard deviations (blue solid curve) calculated using the time series in panel A at different window sizes. The dashed red curve shows a curve-fit based on a Monod equation, green dotted line the half saturation constant (B_0) from the Monod equation, and the purple dotted line the half-saturation constant estimated directly from the blue curve (K_M). τ_d (orange solid line) depicts the dominant timescales as defined in Section 3.2.

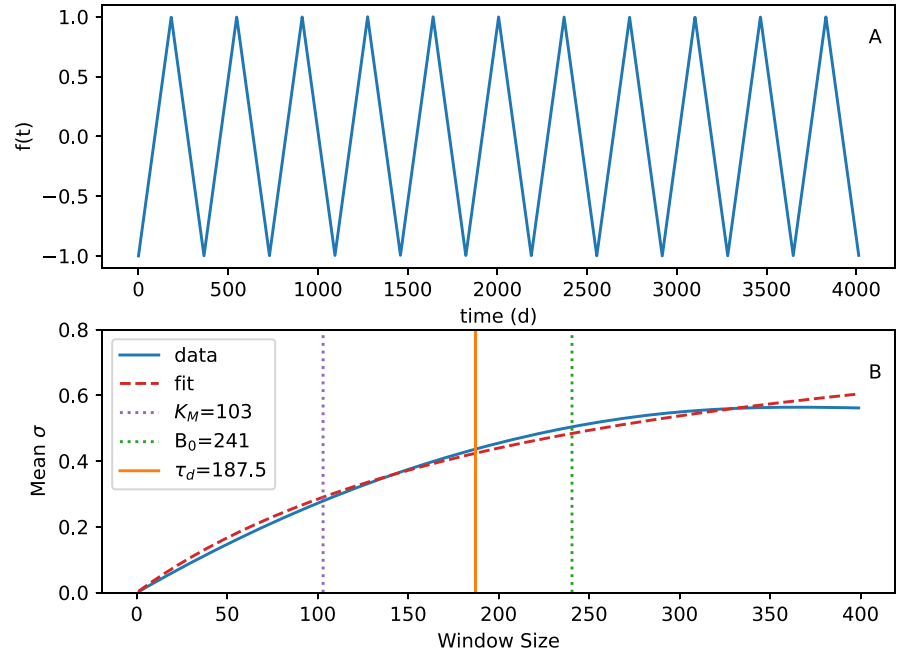

Fig. A.2. Panel A: Time series constructed from a triangle curve with a one year period. Panel B: Mean moving standard deviations (blue solid curve) calculated using the time series in panel A at different window sizes. The dashed red curve shows a curve-fit based on a Monod equation, green dotted line the half saturation constant (B_0) from the Monod equation, and the purple dotted line the half-saturation constant estimated directly from the blue curve (K_M). τ_d (orange solid line) depicts the dominant timescales as defined in Section 3.2.

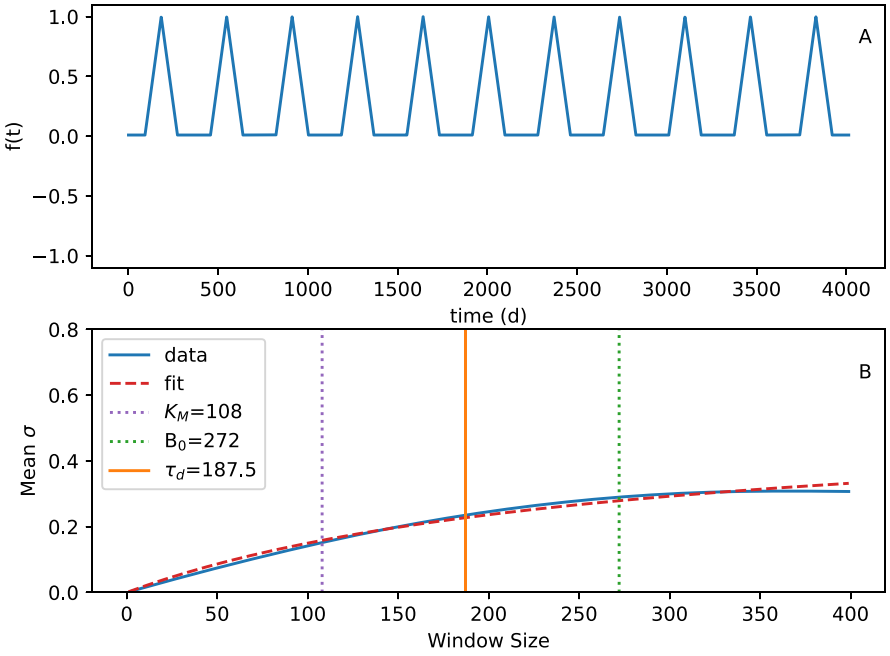

Fig. A.3. Panel A: Time series constructed from a truncated triangle curve with a one year period. Panel B: Mean moving standard deviations (blue solid curve) calculated using the time series in panel A at different window sizes. The dashed red curve shows a curve-fit based on a Monod equation, green dotted line the half saturation constant (B_0) from the Monod equation, and the purple dotted line the half-saturation constant estimated directly from the blue curve (K_M). τ_d (orange solid line) depicts the dominant timescales as defined in Section 3.2.

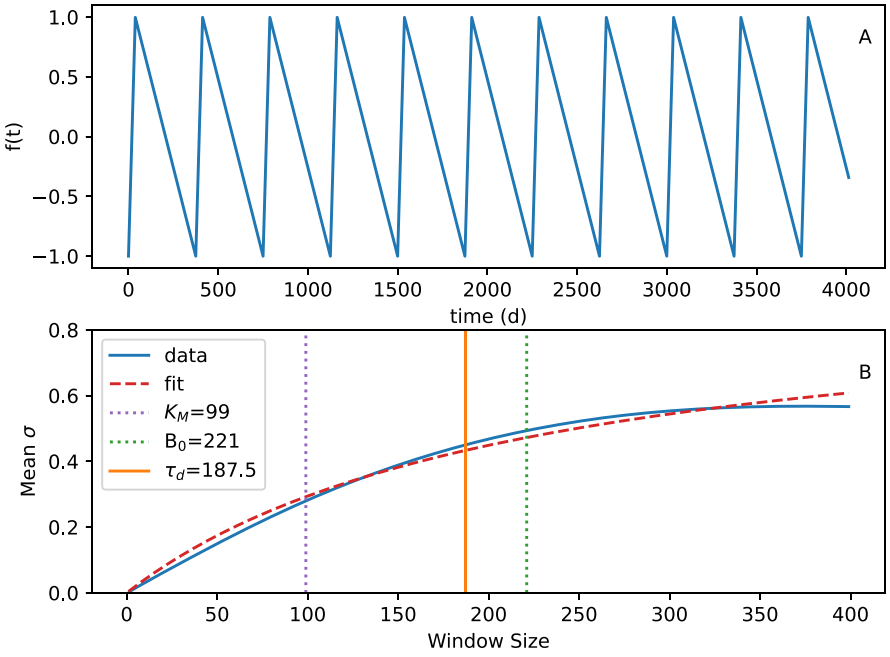

Fig. A.4. Panel A: Time series constructed from a sawtooth curve with a one year period. Panel B: Mean moving standard deviations (blue solid curve) calculated using the time series in panel A at different window sizes. The dashed red curve shows a curve-fit based on a Monod equation, green dotted line the half saturation constant (B_0) from the Monod equation, and the purple dotted line the half-saturation constant estimated directly from the blue curve (K_M). τ_d (orange solid line) depicts the dominant timescales as defined in Section 3.2.

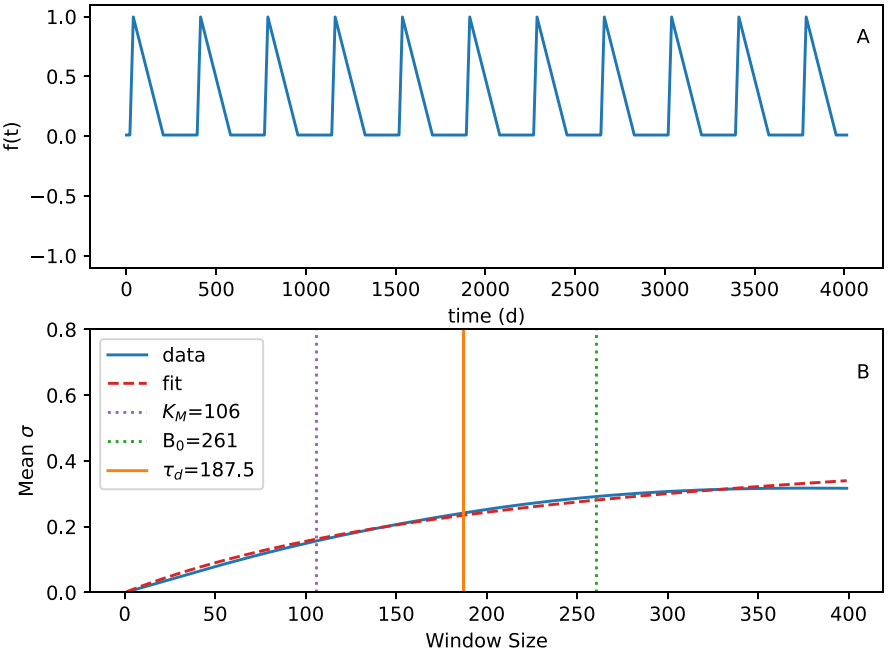

Fig. A.5. Panel A: Time series constructed from a sawtooth triangle curve with a one year period. Panel B: Mean moving standard deviations (blue solid curve) calculated using the time series in panel A at different window sizes. The dashed red curve shows a curve-fit based on a Monod equation, green dotted line the half saturation constant (B_0) from the Monod equation, and the purple dotted line the half-saturation constant estimated directly from the blue curve (K_M). τ_d (orange solid line) depicts the dominant timescales as defined in Section 3.2.

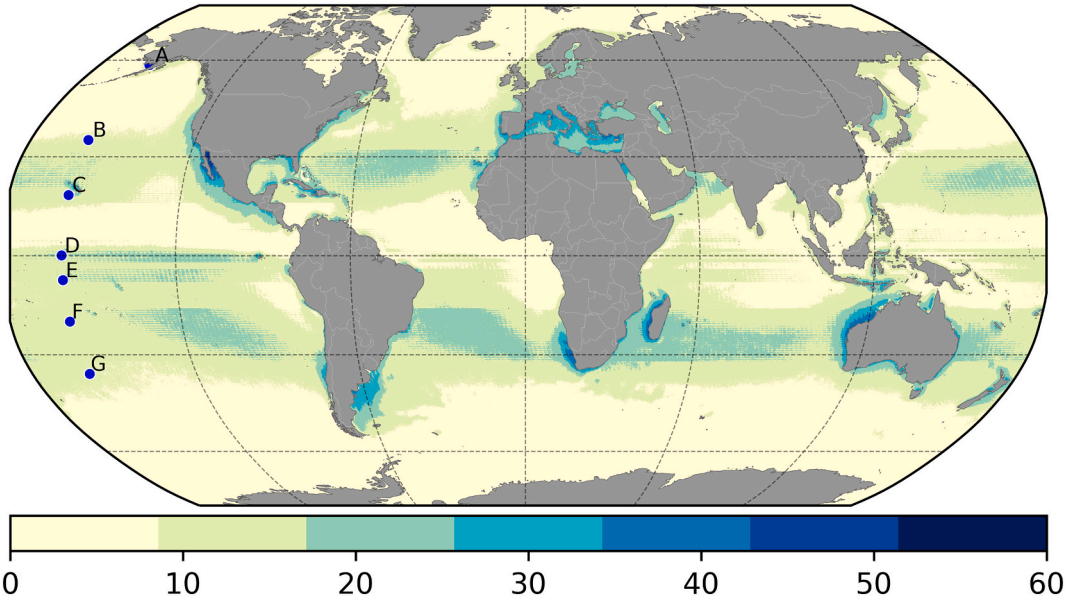

Fig. A.6. Temporal coverage (in percent) of daily data in the NASA-AQUA Chl product for the period 2006–01-01 to 2016–12-31. Blue dots denote locations of the time series in Fig. 4. Labels A-G here corresponds to the panels in Fig. 4.

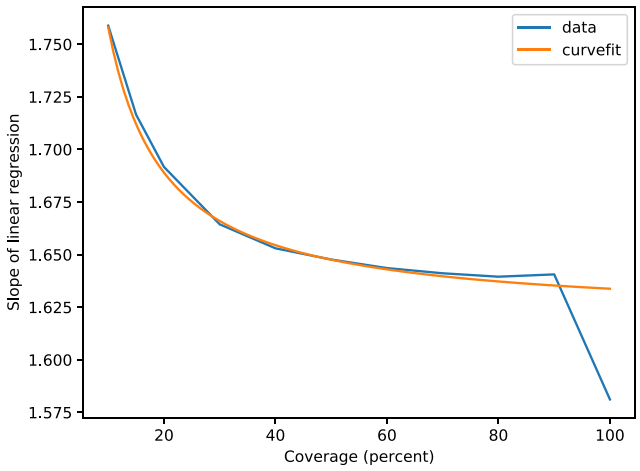

Fig. A.7. Curve fit to identify optimal values for the parameters in Eq. (2).

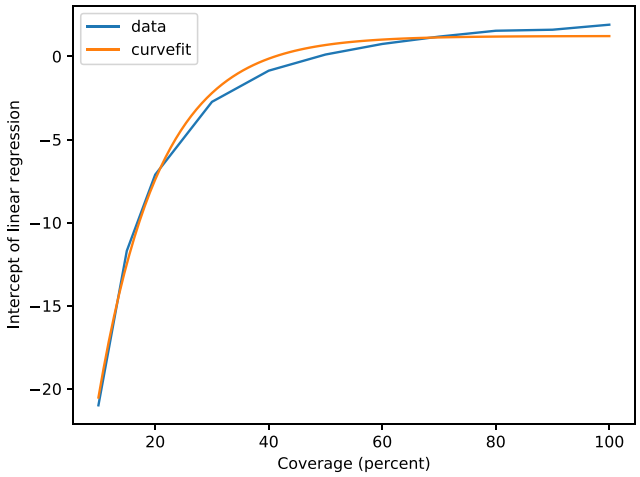

Fig. A.8. Curve fit to identify optimal values for the parameters in Eq. (3).

.

References

Abbott, M.R., Letelier, R.M., 1998. Decorrelation scales of chlorophyll as observed from bio-optical drifters in the california current. Deep Sea Res. Part II: Top. Stud. Oceanogr. 45 (8–9), 1639–1667.

Alkire, M.B., D'Asaro, E., Lee, C., Perry, M.J., Gray, A., Cetinić, I., Briggs, N., Rehm, E., Kallin, E., Kaiser, J., et al., 2012. Estimates of net community production and export using high-resolution, lagrangian measurements of o2, no3-, and poc through the evolution of a spring diatom bloom in the north atlantic. Deep Sea Res. Part I: Oceanogr. Res. Papers 64, 157–174.

Behrenfeld, M.J., Boss, E.S., 2017. Student's tutorial on bloom hypotheses in the context of phytoplankton annual cycles. Glob. Change Biol. 24 (1), 55–77. https://doi.org/10.1111/gcb.13858.

Berger, W.H., Wefer, G., Dec. 1990. Export production: seasonality and intermittency, and paleoceanographic implications. Global Planet. Change 3 (3), 245–254. URL: http://linkinghub.elsevier.com/retrieve/pii/092181819090020D.

Blackwell, S.M., Moline, M.A., Schaffner, A., Garrison, T., Chang, G., 2008. Sub-kilometer length scales in coastal waters. Cont. Shelf Res. 28 (2), 215–226.

Blondeau-Patissier, D., Gower, J.F., Dekker, A.G., Phinn, S.R., Brando, V.E., 2014. A review of ocean color remote sensing methods and statistical techniques for the detection, mapping and analysis of phytoplankton blooms in coastal and open oceans. Prog. Oceanogr. 123, 123–144.

Briggs, N., Perry, M.J., Cetinić, I., Lee, C., D'Asaro, E., Gray, A.M., Rehm, E., 2011. High-resolution observations of aggregate flux during a sub-polar north atlantic spring bloom. Deep Sea Res. Part I: Oceanogr. Res. Papers 58 (10), 1031–1039.

Brown, C.W., Uz, S.S., Corliss, B.H., 2014. Seasonality of oceanic primary production and its interannual variability from 1998 to 2007. Deep Sea Res. Part I: Oceanogr. Res. Papers 90 (C), 166–175. https://doi.org/10.1016/j.dsr.2014.05.009.

Buesseler, K.O., Jun. 1998. The decoupling of production and particulate export in the surface ocean. Global Biogeochem. Cycles 12 (2), 297–310. URL:http://doi.wiley.com/10.1029/97GB03366.

DiTullio, G.R., Grebmeier, J.M., Arrigo, K.R., Lizotte, M.P., Robinson, D.H., Leventer, A., Barry, J.P., VanWoert, M.L., Dunbar, R.B., 2000. 404595a0.html. Nature (News and Views) 404 (6778), 595–598. URL:http://www.nature.com/doifinder/10.1038/35007061.

Doney, S.C., Glover, D.M., McCue, S.J., Fuentes, M., 2003. Mesoscale variability of sea-viewing wide field-of-view sensor (seawifs) satellite ocean color: Global patterns and spatial scales. J. Geophys. Res.: Oceans (1978–2012) 108 (C2) n/a–n/a.

Dunne, J.P., Sarmiento, J.L., Gnanadesikan, A., 2007. A synthesis of global particle export from the surface ocean and cycling through the ocean interior and on the seafloor. Global Biogeochem. Cycles 21 (4), GB4006. URL:http://www.agu.org/pubs/crossref/2007/2006GB002907.shtml.

Dunstan, P.K., Foster, S.D., King, E., Risbey, J., O'Kane, T.J., Monselesan, D., Hobday, A. J., Hartog, J.R., Thompson, P.A., 2018. Global patterns of change and variation in sea surface temperature and chlorophyll a. Sci. Rep. 8 (1), 14624.

Durand, F., Papa, F., Rahman, A., Bala, S.K., 2011. Impact of ganges–brahmaputra interannual discharge variations on bay of bengal salinity and temperature during 1992–1999 period. J. Earth Syst. Sci. 120 (5), 859–872. https://doi.org/10.1007/s12040-011-0118-x.

Fischer, G., Ratmeyer, V., Wefer, G., Jan. 2000. Organic carbon fluxes in the Atlantic and the Southern Ocean: relationship to primary production compiled from satellite radiometer data. Deep-Sea Res. Part Ii-Top. Stud. Oceanogr. 47 (9–11), 1961–1997. URL:http://linkinghub.elsevier.com/retrieve/pii/S0967064500000138.

Giovannoni, S.J., Vergin, K.L., Feb. 2012. Seasonality in Ocean Microbial Communities. Science 335 (6069), 671–676. URL:http://www.sciencemag.org/cgi/doi/10.1126/science.1198078.

Glover, D.M., Doney, S.C., Oestreich, W.K., Tullo, A.W., 2018. Geostatistical analysis of mesoscale spatial variability and error in seawifs and modis/aqua global ocean color data. J. Geophys. Res.: Oceans 123 (1), 22–39.
Good, A., Embury, O., Bulgin, C., Mittaz, J., 2019. Esa sea surface temperature climate change initiative (sst-cci): Level 4 analysis climate data record, version 2.1. URL: http://catalogue.ceda.ac.uk/uuid/62c0f97b1eac4e0197a674870afe1ee6.
Henson, S.A., Dunne, J.P., Sarmiento, J.L., 2009. Decadal variability in north atlantic phytoplankton blooms. J. Geophys. Res.: Oceans (1978–2012) 114 (C4).
Henson, S.A., Sanders, R., Madsen, E., 2012. Global patterns in efficiency of particulate organic carbon export and transfer to the deep ocean. Global Biogeochem. Cycles 26 (1) n/a–n/a. URL:http://onlinelibrary.wiley.com/doi/10.1029/2011GB004099/full.
Hocke, K., Bernet, L., Hagen, J., Murk, A., Renker, M., Mätzler, C., 2019. Diurnal cycle of short-term fluctuations of integrated water vapour above Switzerland. Atmos. Chem. Phys. 19 (19), 12083–12090.
Jackson, T., Sathyendranath, S., Mélin, F., 2017. An improved optical classification scheme for the ocean colour essential climate variable and its applications. Remote Sens. Environ. 203, 152–161. https://doi.org/10.1016/j.rse.2017.03.036.
Jefferson, M., 1938. Standard seasons. Ann. Assoc. Am. Geogr. 28 (1), 1–12. URL:https://www.tandfonline.com/doi/abs/10.1080/00045603809357169.
Jönsson, B.F., Doney, S., Dunne, J., Bender, M.L., 2015. Evaluating southern ocean biological production in two ocean biogeochemical models on daily to seasonal timescales using satellite chlorophyll and o_2) ar observations. Biogeosciences 12 (3), 681–695. URL:https://bg.copernicus.org/articles/12/681/2015/.
Jönsson, B.F., Doney, S.C., Dunne, J., Bender, M., 2013. Evaluation of the southern ocean o2/ar-based ncp estimates in a model framework. J. Geophys. Res.: Biogeosci. 118 (2), 385–399. URL:https://agupubs.onlinelibrary.wiley.com/doi/abs/10.1002/jgrg.20032.
Jönsson, B.F., Salisbury, J.E., Jun. 2016. Episodicity in phytoplankton dynamics in a coastal region. Geophys. Res. Lett. 43 (11), 5821–5828. URL:http://doi.wiley.com/10.1002/2016GL068683.
Jönsson, B.F., Sathyendranath, S., Platt, T., 2020. Trends in winter light environment over the arctic ocean: A perspective from two decades of ocean color data. Geophys. Res. Lett. 47 (16), e2020GL089037. URL:https://agupubs.onlinelibrary.wiley.com/doi/abs/10.1029/2020GL089037.
Journel, A.G., Huijbregts, C.J., 1978. Mining geostatistics, vol. 600. Academic press, London.
Keerthi, M.G., Levy, M., Aumont, O., Lengaigne, M., Antoine, D., 2020. Contrasted contribution of intraseasonal time scales to surface chlorophyll variations in a bloom and an oligotrophic regime. J. Geophys. Res.: Oceans 125 (5), e2019JC015701.
Lee, Z., Jiang, M., Davis, C., Pahlevan, N., Ahn, Y.-H., Ma, R., 2012. Impact of multiple satellite ocean color samplings in a day on assessing phytoplankton dynamics. Ocean Sci. J. 47 (3), 323–329.
Legaard, K.R., Thomas, A.C., 2007. Spatial patterns of intraseasonal variability of chlorophyll and sea surface temperature in the california current. J. Geophys. Res.: Oceans (1978–2012) 112 (C9).
Legendre, L., Jan. 1990. The significance of microalgal blooms for fisheries and for the export of particulate organic carbon in oceans. J. Plankton Res. 12 (4), 681–699. URL:https://academic.oup.com/plankt/article-lookup/doi/10.1093/plankt/12.4.681.
Longhurst, A., Sathyendranath, S., Platt, T., Caverhill, C., 1995. An Estimate of Global Primary Production in the Ocean From Satellite Radiometer Data. J. Plankton Res. 17 (6), 1245–1271. URL:http://plankt.oxfordjournals.org/cgi/doi/10.1093/plankt/17.6.1245.
Longhurst, A.R., 2007. Ecological geography of the sea. Elsevier.
Lutz, M.J., Caldeira, K., Dunbar, R.B., Behrenfeld, M.J., 2007. Seasonal rhythms of net primary production and particulate organic carbon flux to depth describe the efficiency of biological pump in the global ocean. J. Geophys. Res.-Oceans 112. –. URL:http://links.isiglobalnet2.com/gateway/Gateway.cgi?GWVersion=2&SrcAuth=mekentosj&SrcApp=Papers&DestLinkType=FullRecord&DestApp=WOS&KeyUT=000250220100001.
Mahadevan, A., 2016. The impact of submesoscale physics on primary productivity of plankton. Ann. Rev. Mar. Sci. 8 (1), 1–24.
Mahadevan, A., Campbell, J., 2002. Biogeochemical patchiness at the sea surface. Geophys. Res. Lett. 29 (19), 32-1–32-4.
Martin, P., Lampitt, R.S., Perry, M.J., Sanders, R., Lee, C., D'Asaro, E., 2011. Export and mesopelagic particle flux during a north atlantic spring diatom bloom. Deep Sea Res. Part I: Oceanogr. Res. Papers 58 (4), 338–349.
McClain, C.R., 2009. A decade of satellite ocean color observations*. Mar. Sci. 1 (1), 19–42.
Mélin, F., Vantrepotte, V., Chuprin, A., Grant, M., Jackson, T., Sathyendranath, S., 2017. Assessing the fitness-for-purpose of satellite multi-mission ocean color climate data records: A protocol applied to OC-CCI chlorophyll- a data. Remote Sens. Environ. 203, 139–151. https://doi.org/10.1016/j.rse.2017.03.039.
Merchant, C., Embury, O., Roberts-Jones, J., Fiedler, E., Bulgin, C., Corlett, G., Good, S., McLaren., A., Rayner, N., Donlon, C., 2016. Esa sea surface temperature climate change initiative (esa sst cci): Analysis long term product version 1.1. URL:http://catalogue.ceda.ac.uk/uuid/c65ce27928f34ebd92224c451c2a8bed.
Merchant, C.J., Embury, O., Bulgin, C.E., Block, T., Corlett, G.K., Fiedler, E., Good, S.A., Mittaz, J., Rayner, N.A., Berry, D., et al., 2019. Satellite-based time-series of sea-surface temperature since 1981 for climate applications. Sci. Data 6 (1), 223.
Monod, J., 1949. The growth of bacterial cultures. Annu. Rev. Microbiol. 3 (1), 371–394. https://doi.org/10.1146/annurev.mi.03.100149.002103.
Moore, T.S., Campbell, J.W., Dowell, M.D., 2009. A class-based approach to characterizing and mapping the uncertainty of the MODIS ocean chlorophyll product. Remote Sens. Environ. 113 (11), 2424–2430. https://doi.org/10.1016/j.rse.2009.07.016.
Moore, T.S., Dowell, M.D., Franz, B.A., 2012. Detection of coccolithophore blooms in ocean color satellite imagery: A generalized approach for use with multiple sensors. Remote Sens. Environ. 117, 249–263. https://doi.org/10.1016/j.rse.2011.10.001.
Muller-Karger, F., Varela, R., Thunell, R., Scranton, M., Bohrer, R., Taylor, G., Capelo, J., Astor, Y., Tappa, E., Ho, T.Y., Walsh, J.J., 2001. Annual cycle of primary production in the Cariaco Basin: Response to upwelling and implications for vertical export. J. Geophys. Res.: Oceans (1978–2012) 106 (C3), 4527–4542. URL:http://onlinelibrary.wiley.com/doi/10.1029/1999JC000291/abstract.
Oliver, H., Zhang, W.G., Smith Jr, W.O., Alatalo, P., Chappell, P.D., Hirzel, A.J., Selden, C.R., Sosik, H.M., Stanley, R.H., Zhu, Y., et al., 2021. Diatom hotspots driven by western boundary current instability. Geophys. Res. Lett., e2020GL091943
Platt, T., Fuentes-Yaco, C., Frank, K.T., 2003. Spring algal bloom and larval fish survival. Nature 423 (6938), 398–399.
Prend, C.J., Keerthi, M.G., Lévy, M., Aumont, O., Gille, S.T., Talley, L.D., 2022. Sub-seasonal forcing drives year-to-year variations of southern ocean primary productivity. Global Biogeochem. Cycles 36 (7), e2022GB007329.
Raspaud, M., Hoese, D., Lahtinen, P., Dybbroe, A., Finkensieper, S., Roberts, W., Rasmussen, L. Ø., Proud, S., Joro, S., Daruwala, R., Holl, G., Jasmin, T., BENR0, Leppelt, T., Egede, U., R.K.Garcia, Itkin, M., LTMeyer, Sigurðsson, E., Radar, S., Division, N., Aspenes, T., Hazbottles, ColinDuff, Joleenf, Cody, Clementi, L., Honnorat, M., Schulz, H., Hatt, B., Valentino, A., 2019. pytroll/satpy: Version 0.16.0. URL:https://zenodo.org/record/3250583.
Sathyendranath, S., Brewin, R., Brockmann, C., Brotas, V., Calton, B., Chuprin, A., Cipollini, P., Couto, A., Dingle, J., Doerffer, R., Donlon, C., Dowell, M., Farman, A., Grant, M., Groom, S., Horseman, A., Jackson, T., Krasemann, H., Lavender, S., Martinez-Vicente, V., Mazeran, C., Mélin, F., Moore, T., Müller, D., Regner, P., Roy, S., Steele, C., Steinmetz, F., Swinton, J., Taberner, M., Thompson, A., Valente, A., Zühlke, M., Brando, V., Feng, H., Feldman, G., Franz, B., Frouin, R., Gould, R., Hooker, S., Kahru, M., Kratzer, S., Mitchell, B., Muller-Karger, F., Sosik, H., Voss, K., Werdell, J., Platt, T., Oct. 2019. An ocean-colour time series for use in climate studies: The experience of the ocean-colour climate change initiative (OC-CCI). Sensors 19 (19), 4285.
Sathyendranath, S., Jackson, T., Brockmann, C., Brotas, V., Calton, B., Chuprin, A., Clements, O., Cipollini, P., Danne, O., Dingle, J., Donlon, C., Grant, M., Groom, S., Krasemann, H., Lavender, S., Mazeran, C., Mélin, F., Moore, T.S., Müller, D., Regner, P., Steinmetz, F., Steele, C., Swinton, J., Valente, A., Zühlke, M., Feldman, G., Franz, B., Frouin, R., Werdell, J., Platt, T., 2020. Esa ocean colour climate change initiative (ocean_colour_cci): Version 4.2 data. URL:https://catalogue.ceda.ac.uk/uuid/d62f7f801cb54c749d20e736d4a1039f.
Scharek, R., Tupas, L.M., Karl, D.M., 1999. Diatom fluxes to the deep sea in the oligotrophic North Pacific gyre at Station ALOHA. Mar. Ecol. - Prog. Series 182, 55–67. URL:http://www.int-res.com/abstracts/meps/v182/p55-67/.
Siegel, D., Behrenfeld, M., Maritorena, S., McClain, C., Antoine, D., Bailey, S., Bontempi, P., Boss, E., Dierssen, H., Doney, S., et al., 2013. Regional to global assessments of phytoplankton dynamics from the seawifs mission. Remote Sens. Environ. 135, 77–91.
Steinmetz, F., Deschamps, P.-Y., Ramon, D., 2011. Atmospheric correction in presence of sun glint: application to MERIS. Opt. Express 19 (10), 9783. https://doi.org/10.1364/oe.19.009783.
Stramska, M., Dickey, T.D., 1993. Phytoplankton bloom and the vertical thermal structure of the upper ocean. J. Mar. Res. 51 (4), 819–842.
Sundby, S., Drinkwater, K.F., Kjesbu, O.S., 2016. The north atlantic spring-bloom system—where the changing climate meets the winter dark. Front. Mar. Sci. 3, 28.
Sverdrup, H., 1953. On conditions for the vernal blooming of phytoplankton. J. Cons. Int. Explor. Mer 18 (3), 287–295.
Trenberth, K.E., 1983. What are the seasons? Bull. Am. Meteorol. Soc. 64 (11), 1276–1282.
Virtanen, P., Gommers, R., Oliphant, T.E., Haberland, M., Reddy, T., Cournapeau, D., Burovski, E., Peterson, P., Weckesser, W., Bright, J., van der Walt, S.J., Brett, M., Wilson, J., Millman, K.J., Mayorov, N., Nelson, A.R.J., Jones, E., Kern, R., Larson, E., Carey, C.J., Polat, İ., Feng, Y., Moore, E.W., VanderPlas, J., Laxalde, D., Perktold, J., Cimrman, R., Henriksen, I., Quintero, E.A., Harris, C.R., Archibald, A.M., Ribeiro, A.H., Pedregosa, F., van Mulbregt, P., 2020. SciPy 1.0 Contributors, 2020. SciPy 1.0: Fundamental Algorithms for Scientific Computing in Python. Nat. Methods 17, 261–272.
Weibull, W., 1951. A statistical distribution function of wide applicability. J. Appl. Mech.
Yoder, J.A., Kennelly, M.A., 2003. Seasonal and enso variability in global ocean phytoplankton chlorophyll derived from 4 years of seawifs measurements. Global Biogeochem. Cycles 17 (4) n/a–n/a.
Zingone, A., Phlips, E.J., Harrison, P.J., 2010. Multiscale variability of twenty-two coastal phytoplankton time series: a global scale comparison. Estuaries Coast. 33 (2), 224–229.